

Timmons, Nicholas and Cooray, A. and Riechers, D.A. and Nayyeri, H. and Fu, Hai and Jullo, Eric and Gladders, Michael D. and Baes, Maarten and Bussmann, R.S. and Calanog, Jae and Clements, D.L. and da Cunha, E. and Dye, S. and Eales, S.A. and Furlanetto, C. and Gonzalez-Nuevo, J. and Greenslade, J. and Gurwell, M. and Messias, Hugo and Michalowski, M.J. and Oteo, I. and Pérez-Fournón, I. and Scott, Douglas and Valiante, E. (2016) Multi-wavelength lens construction of a Planck and Herschel-detected star-bursting galaxy. *Astrophysical Journal*, 829 (1). pp. 1-11. ISSN 1538-4357

Access from the University of Nottingham repository:

http://eprints.nottingham.ac.uk/42360/1/Timmons_2016_ApJ_829_21.pdf

Copyright and reuse:

The Nottingham ePrints service makes this work by researchers of the University of Nottingham available open access under the following conditions.

This article is made available under the University of Nottingham End User licence and may be reused according to the conditions of the licence. For more details see: http://eprints.nottingham.ac.uk/end_user_agreement.pdf

A note on versions:

The version presented here may differ from the published version or from the version of record. If you wish to cite this item you are advised to consult the publisher's version. Please see the repository url above for details on accessing the published version and note that access may require a subscription.

For more information, please contact eprints@nottingham.ac.uk



MULTI-WAVELENGTH LENS RECONSTRUCTION OF A *PLANCK* AND *HERSCHEL*-DETECTED STAR-BURSTING GALAXY

NICHOLAS TIMMONS¹, ASANTHA COORAY¹, DOMINIK A. RIECHERS², HOOSHANG NAYYERI¹, HAI FU³, ERIC JULLO⁴,
MICHAEL D. GLADDERS⁵, MAARTEN BAES⁶, R. SHANE BUSSMANN², JAE CALANOG⁷, DAVID L. CLEMENTS⁸, ELISABETE DA CUNHA⁹,
SIMON DYE¹⁰, STEPHEN A. EALES¹¹, CRISTINA FURLANETTO^{10,12}, JOAQUIN GONZALEZ-NUÑO¹³, JOSHUA GREENSLADE⁸,
MARK GURWELL¹⁴, HUGO MESSIAS¹⁵, MICHAŁ J. MICHAŁOWSKI¹⁶, IVÁN OTEO^{16,17}, ISMAEL PÉREZ-FOURNON^{18,19},
DOUGLAS SCOTT²⁰, AND ELISABETTA VALIANTE¹¹

¹ Department of Physics and Astronomy, University of California, Irvine, CA 92697, USA

² Department of Astronomy, Cornell University, Ithaca, NY 14853, USA

³ Department of Physics & Astronomy, University of Iowa, Iowa City, IA 52242, USA

⁴ Aix-Marseille Université, CNRS, LAM (Laboratoire d'Astrophysique de Marseille) UMR 7326, 38 rue Joliot-Curie, F-13388 Marseille Cedex, France

⁵ The Department of Astronomy and Astrophysics, and the Kavli Institute for Cosmological Physics, The University of Chicago, 5640 South Ellis Avenue, Chicago, IL 60637, USA

⁶ Sterrenkundig Observatorium, Universiteit Gent, Krijgslaan 281S9, B-9000 Gent, Belgium

⁷ Department of Physical Sciences, San Diego Miramar College, San Diego, CA 92126, USA

⁸ Physics Department, Blackett Lab, Imperial College, Prince Consort Road, London SW7 2AZ, UK

⁹ Centre for Astrophysics and Supercomputing, Swinburne University of Technology, Hawthorn, Victoria 3122, Australia

¹⁰ School of Physics and Astronomy, The University of Nottingham, University Park, Nottingham, NG7 2RD, UK

¹¹ School of Physics and Astronomy, Cardiff University, Queens Buildings, The Parade, Cardiff CF24 3AA, UK

¹² CAPES Foundation, Ministry of Education of Brazil, Brasília/DF, 70040-020, Brazil

¹³ Departamento de Física, Universidad de Oviedo, C. Calvo Sotelo s/n, E-33007 Oviedo, Spain

¹⁴ Harvard-Smithsonian Center for Astrophysics, 60 Garden Street, Cambridge, MA 02138, USA

¹⁵ Instituto de Astrofísica e Ciências do Espaço, Universidade de Lisboa, OAL, Tapada da Ajuda, PT 1349-018 Lisboa, Portugal

¹⁶ Institute for Astronomy, Royal Observatory, Blackford Hill, Edinburgh, EH9 3HJ, UK

¹⁷ European Southern Observatory, Karl-Schwarzschild-Str. 2, D-85748 Garching, Germany

¹⁸ Instituto de Astrofísica de Canarias (IAC), E-38200 La Laguna, Tenerife, Spain

¹⁹ Departamento de Astrofísica, Universidad de La Laguna, E-38206, La Laguna, Tenerife, Spain

²⁰ Department of Physics & Astronomy, University of British Columbia, 6224 Agricultural Road, Vancouver, BC V6T 1Z1, Canada

Received 2015 December 9; revised 2016 July 14; accepted 2016 July 15; published 2016 September 16

ABSTRACT

We present a source-plane reconstruction of a *Herschel* and *Planck*-detected gravitationally lensed dusty star-forming galaxy (DSFG) at $z = 1.68$ using *Hubble*, Submillimeter Array (SMA), and Keck observations. The background submillimeter galaxy (SMG) is strongly lensed by a foreground galaxy cluster at $z = 0.997$ and appears as an arc with a length of $\sim 15''$ in the optical images. The continuum dust emission, as seen by SMA, is limited to a single knot within this arc. We present a lens model with source-plane reconstructions at several wavelengths to show the difference in magnification between the stars and dust, and highlight the importance of multi-wavelength lens models for studies involving lensed DSFGs. We estimate the physical properties of the galaxy by fitting the flux densities to model spectral energy distributions leading to a magnification-corrected star-formation rate (SFR) of $390 \pm 60 M_{\odot} \text{ yr}^{-1}$ and a stellar mass of $1.1 \pm 0.4 \times 10^{11} M_{\odot}$. These values are consistent with high-redshift massive galaxies that have formed most of their stars already. The estimated gas-to-baryon fraction, molecular gas surface density, and SFR surface density have values of 0.43 ± 0.13 , $350 \pm 200 M_{\odot} \text{ pc}^{-2}$, and $\sim 12 \pm 7 M_{\odot} \text{ yr}^{-1} \text{ kpc}^{-2}$, respectively. The ratio of SFR surface density to molecular gas surface density puts this among the most star-forming systems, similar to other measured SMGs and local ULIRGs.

Key words: cosmology: observations – galaxies: evolution – infrared: galaxies – submillimeter: galaxies

1. INTRODUCTION

In recent years, large area far-infrared and submillimeter surveys, for example, the *Herschel*-Astrophysical TeraHertz Large Area Survey (H-ATLAS; Eales et al. 2010), have allowed the efficient selection of gravitationally lensed high- z dusty star-forming galaxies (DSFGs; e.g., Negrello et al. 2007, 2010; González-Núñez et al. 2012; Bussmann et al. 2013; Wardlow et al. 2013; Nayyeri et al. 2016). These DSFGs (see Casey et al. 2014 for a recent review) have star-formation rates (SFRs) of $\sim 10^2$ – $10^3 M_{\odot} \text{ yr}^{-1}$, with typical stellar masses of $\sim 10^{11}$ – $10^{12} M_{\odot}$, and are generally found during the peak epoch of galaxy formation and evolution at $z \sim 1$ – 4 . Such rapid star formation has a short lifetime (< 0.1 Gyr) and is rare in the local universe (Tacconi et al. 2010). Luminous and ultra-luminous infrared galaxies (LIRGs and ULIRGs), of which

DSFGs are an analog, contribute significantly ($\sim 70\%$) to the cosmic star formation at $z = 1$ (Le Floc'h et al. 2005). Recent studies have shown that DSFGs may differ from ULIRGs in that their star-forming regions may be more spatially extended (e.g., Younger et al. 2008; Ivison et al. 2011; Riechers et al. 2011). There is evidence to suggest DSFGs are likely an early stage of today's massive elliptical galaxies (e.g., Lilly et al. 1999; Swinbank et al. 2006; Lapi et al. 2011; Fu et al. 2013). DSFGs are usually faint at rest-frame optical wavelengths due to dust obscuration, but are bright in the rest-frame far-IR, making submillimeter surveys the perfect tool to study DSFGs (Negrello et al. 2010).

While wide area surveys with *Herschel* and ground-based instruments have increased the sample sizes of DSFGs at submillimeter wavelengths, due to limitations associated with

existing instruments in sensitivity and spatial resolution, our ability to conduct detailed investigations on the physical properties of DSFGs has been severely hampered. Thankfully, strong gravitational lensing can be used to overcome these limitations. The flux amplification as a result of gravitational lensing allows for the detection of otherwise intrinsically fainter dust obscured galaxies and the associated spatial enhancement allows spatially resolved imaging observations with existing facilities (e.g., Fu et al. 2012; Messias et al. 2014).

H-ATLAS J132427.0+284452 (hereafter HATLAS J132427) peaks at $350\ \mu\text{m}$ with a flux density of $\sim 380 \pm 8\ \text{mJy}$ (from *Herschel* Spectral and Photometric Imaging Receiver, SPIRE). It is also identified in the all-sky maps from *Planck* (Planck Collaboration et al. 2011) as PLCKERC857 G047.32+82.53 ($1.3 \pm 0.15\ \text{Jy}$) at 857 GHz ($350\ \mu\text{m}$) in the *Planck* Early Release Compact Source Catalog (Planck Collaboration et al. 2011). Although the *Planck*-detected flux density is $\sim 4\times$ larger than the *Herschel*/SPIRE measurement in H-ATLAS, the difference can be explained as due to the large 3–5 arcmin beam of *Planck* measurements, which may cause blending in an over-dense field. Such a difference is also present in a previous *Planck*-detected H-ATLAS lensed source. H-ATLAS J114637.9-001132 (Fu et al. 2012) is detected by *Planck* with a flux density of $S_{350} = 2.1 \pm 0.8\ \text{Jy}$, but in *Herschel* the flux density is measured to be $S_{350} = 378 \pm 28\ \text{mJy}$ corresponding to a $\sim 5\times$ larger *Planck* flux density much like HATLAS J132427. Despite the *Planck* flux being uncertain, the detection is validated through other observations and confirms *Planck*'s ability to detect the brightest lensed DSFGs (see Canameras et al. 2015).

In this paper, we present new *Hubble Space Telescope* (*HST*), SCUBA2, and Keck observations of HATLAS J132427 along with previous multi-wavelength observations to create a complete profile of this *Planck*- and *Herschel*-detected DSFG. In Section 2, we describe the observations and data reduction procedures. In Section 3, we describe previous and archival observations used in the analysis. In Section 4, we use high-resolution imaging to construct a lens model and calculate the magnification factors. In Section 5, we model the spectral energy distribution (SED) and derive physical properties from the fit. In Section 6, we discuss the derived properties of HATLAS J132427 and compare them to other SMGs and DSFGs. We conclude with a summary in Section 7. Throughout, we make use of the standard flat- Λ CDM cosmological model with $H_0 = 70\ \text{km s}^{-1}\ \text{Mpc}^{-1}$ and $\Omega_\Lambda = 0.73$.

2. OBSERVATIONS

Early observations of HATLAS J132427 are presented in George et al. (2013). Here we present new Keck, SCUBA2, *Hubble*/WFC3 imaging data and *Hubble*/WFC3 grism observations. Figure 1 shows a three color image of the source using *HST* (F105W and F160W bands) and Keck (K_s band) imaging along with SMA contours overlaid to show the spatial variations of the source at different wavelengths. Figure 2 shows Keck NIRC2 K_s -band imaging with the critical and caustic lines used in the lens model.

2.1. Keck/NIRC2

We obtained a 1680 s exposure in H band with an airmass of 1.02 and a 3840 s exposure in K_s band with an airmass of 1.36 (PI: Cooray) on 2012 February 4 with the Keck II/NIRC2

instrument aided with the laser guide-star adaptive optics system (LGSAO; Wizinowich et al. 2006). The imaging observations made use of a pixel scale at $0''.04\ \text{pixel}^{-1}$ for both filters. Custom IDL scripts were used to reduce the data following the procedures in Fu et al. (2012, 2013), which includes a dark subtraction, bad pixel masking, background subtraction, as well as flat-fielding. The K_s -band image was flux calibrated using UKIDSS (Lawrence et al. 2007) K -band photometry. The H -band image was flux calibrated using a common set of bright stars detected in NIRC2 image and in the *Hubble*/WFC3 F160W band image.

2.2. Hubble/WFC3

Hubble/WFC3 observations of HATLAS J132427 were completed with three orbits under GO program 13399 in Cycle 21 (PI: Cooray). We obtained a total of 10 exposures including 2 direct images (F105W and F160W) and 8 grism observations. The F105W observation had a total exposure time of 453 s while the F160W observation had a total exposure time of 353 s. Six of the grism observations were taken with the G102 (800 nm–1150 nm) grism for a total exposure time of 5218 s. The remaining two grism observations were taken with the G141 (1075–1700 nm) grism for a total exposure time of 2406 s.

We made use of the calibrated *HST* imaging and grism data from the CALWF3 reduction pipeline, as provided by the Space Telescope Science Institute.²¹ The spectra for individual objects in the image were extracted with the aXe software package (Kümmel et al. 2009). The data products include the two-dimensional combined grism stamp for each object as well as flux-calibrated one-dimensional spectra, contamination estimates, and error estimates. Similar analysis and reduction steps for the other target, (HATLASJ1429-0028) in GO program 13399 in Cycle 21 are described in Timmons et al. (2015).

The top portion of Figure 3 shows the direct imaging for the F105W and F160W filters aligned so that the dispersion direction of the grism is horizontal. Figure 3 also shows the two-dimensional stamps for the two grism filters. The bottom portion of Figure 3 shows the extracted one-dimensional spectra for each grism filter with a close up view of the two-dimensional continuum shown as an inset. The 2D stamp and the 1D spectra come from the bright northern clump as can be seen in Figure 3. Only the northern clump had a detectable continuum that was not overly contaminated by other spectra in the field. This clump has been circled in blue in the F105W and F160W images in Figure 3. The expected emission lines at $z = 1.68$ are shown in the 1D spectra of Figure 3 and it is clear there is no significant line detection in either of the grism spectra, and so we cannot conduct line ratio diagnostics on HATLAS J132427. This is due to the low surface brightness of the galaxy compared to the source detected in Timmons et al. (2015), which involved bright multiply imaged star-forming knots. Unfortunately, due to the overlapping grism spectra from nearby galaxies, we cannot integrate longer to improve the signal-to-noise of the spectrum from our target.

²¹ www.stsci.edu/hst/wfc3/pipeline/wfc3_pipeline

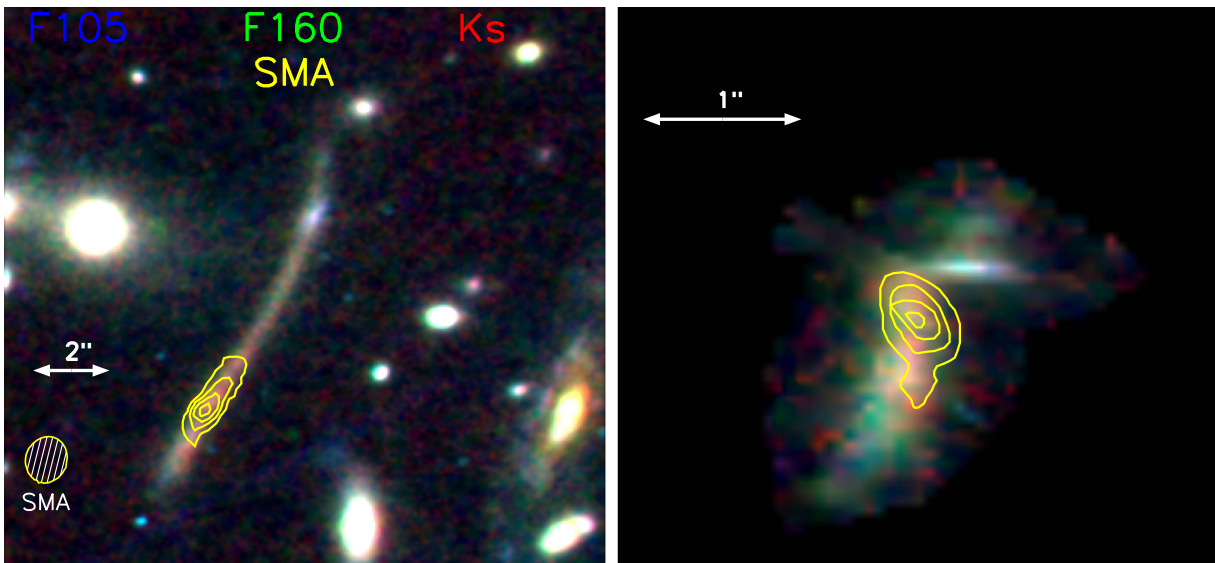


Figure 1. Left: three color image of HATLAS J132427+284452 using *Hubble*/WFC3 F105W (blue) and F160W (green), and Keck NIRC2 K_s (red) bands with Submillimeter Array (SMA) 870 μm band emission contours are overlaid. The SMA contours are at 3σ , 6σ , 9σ , and 12σ , where σ is the rms noise ($0.6 \text{ mJy beam}^{-1}$). The dust emission, and thus the *Herschel* and primary *Planck* source, associated with the DSFG is concentrated in the area of the yellow contours while the optical emission extends over an arc of $\sim 15''$. For reference, we show the SMA beam in the bottom left. Right: three color source-plane reconstruction with SMA source-plane contours overlaid with the same contouring steps as in the left panel (see Section 4 for the lens reconstruction). The spatial resolution of the reconstruction is $\sim 0''.06 \text{ pixel}^{-1}$ or $\sim 0.5 \text{ kpc pixel}^{-1}$.

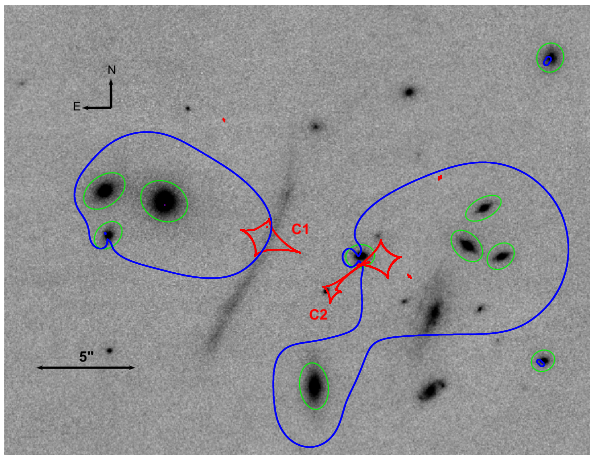


Figure 2. Keck/NIRC2 K_s -band image with the critical and caustic (C1 and C2) lines over-plotted in blue and red, respectively. Circled in green are the foreground lens galaxies used in constructing the lens model. In addition to individual galaxies, the lensing reconstruction requires extended potential associated with the two galaxy groups/clusters to the east and west of the lensing arc.

2.3. SCUBA2

This source, and the field around it, was observed by the SCUBA2 bolometer array camera on the JCMT (Holland et al. 2013). These observations were part of a broader program following up sources in the H-ATLAS survey (M13AU12, PI D.L. Clements). The observations of the field around HATLAS J132427 were made on 2013 April 8th and 12th using the standard pseudo-circular DAISY observing sequence for small and compact sources. This provides maps of a circular region of roughly 350 arcseconds in radius around the target position. The integration time in this field is a function of position, with the central regions receiving greater integration time than the outer regions. Five separate DAISY maps of HATLAS

J132427 were made, three on April 8th and two on April 12th. The conditions for these observations were rated grade 3, indicating $\tau_{225 \text{ GHz}}$ 0.08–0.12. These conditions are adequate for 850 μm observations but not for good 450 μm photometry.

The data were reduced in the standard manner using the SMURF software provided by the observatory. The SMURF iterative mapmaker *makemap* produced individual maps for each of the five subintegrations using the reduction recipe optimized for blank fields with corrections for atmospheric opacity. The five resulting maps were then combined using the mosaic tool to produce a final image which was then match filtered to optimize the signal-to-noise ratio (S/N) of unresolved sources. The final image was then trimmed to produce a 350 arcsecond radius field. The final map has a total integration time of 1850 s at its center, where HATLAS J132427 is located, falling to 450 s at the edges. HATLAS J132427 is detected at the center of the final images with an 850 μm S/N ratio of ~ 30 and a flux of $43 \pm 1.2 \text{ mJy}$. It is interesting to note that five other 850 μm sources are detected at $>4\sigma$ in the final map, suggesting the presence of a moderate over-density of submillimeter sources around HATLAS J132427.

3. PREVIOUS AND ARCHIVAL OBSERVATIONS

HATLAS J132427 was first reported as a candidate strongly lensed giant arc at optical wavelengths in Gladders et al. (2003) and its discovery and follow-up as a bright source in *Herschel* data is discussed in George et al. (2013). The following is a summary of previous or archival observations that were used for the present analysis. The flux densities are shown in Table 2.

Herschel Photoconductor Array Camera and Spectrometer (PACS; Poglitsch et al. 2010) data at 100 μm and 160 μm were collected as a part of the OT1 program (OT_RIVISON_1). The total integration time of 360 s reaching $\sigma \sim 10 \text{ mJy}$ for 100 μm and $\sigma \sim 12 \text{ mJy}$ for 160 μm . *Herschel*/SPIRE Fourier

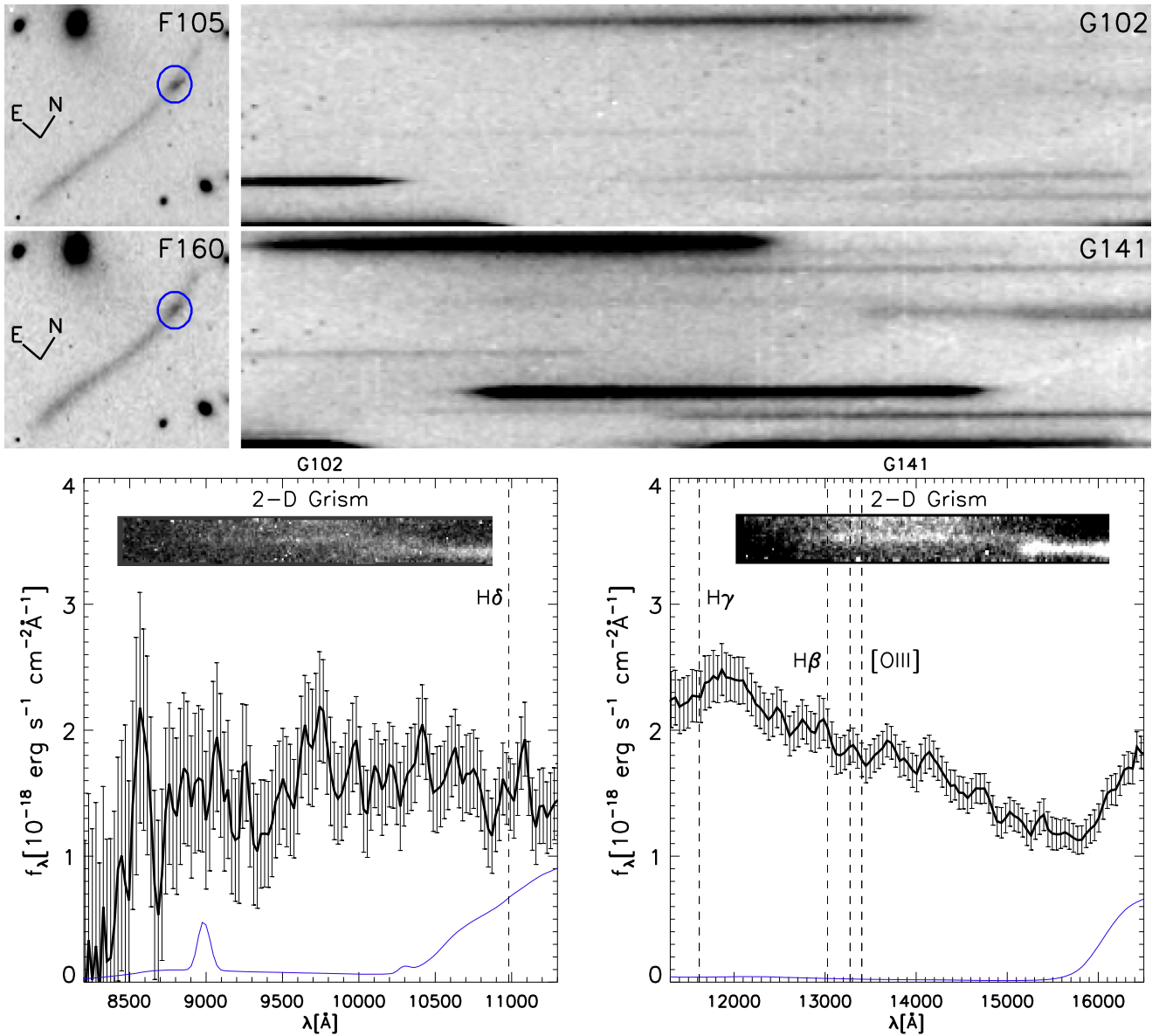


Figure 3. Top left: the direct image in each of the WFC3 imaging filters oriented so that the dispersion direction of the grism is horizontal. Top right: the two-dimensional grism images of HATLAS J132427. The top panel shows G102 and F105W images while the middle panel shows G141 and F160W images. Bottom: the extracted 1D spectra from the G102 and G141 slit-less spectra. The blue line is the estimated contamination coming from other spectra in the field. The 2D grism stamps are inlayed with vertical lines corresponding to useful emission lines over-plotted. Despite the presence of continuum emission no emission lines were detected. Due to contamination from other spectra in the field only the bright northern clump, which has been circled in blue, had an extractable continuum. It was not possible to extract a 1D spectrum from the southern clump associated with the radio detection.

Table 1
Observed Properties

Parameter	Value
R.A., Decl.	13:24:27.206 + 28:44:49.40
z_{source}	1.676 ± 0.001
z_{lens}	0.997 ± 0.017

Transform Spectrometer (FTS; Griffin et al. 2010) observations were completed on 2012 August 2. The wavelength coverage was $\lambda_{\text{obs}} = 194 - 671 \mu\text{m}$ and the total observing time was 3.8 hr. The data resulted in the discovery of the bright [C II]/158 μm emission line with a peak flux density of ~ 0.8 Jy, allowing the redshift of $z = 1.68$ to be measured directly, for the first time, from far-infrared spectroscopy. While the

PACS data are used for the SED analysis the FTS spectrum is not. It is shown in Figure 6 but is not used in the SED analysis due to the presence of the bright [C II]158 μm emission line.

As a part of program 2011B-S044, 870 μm imaging data were taken with the Submillimeter Array (SMA; PI: Bussmann). The total integration time of 9.7 hr was taken in the compact, extended, and very extended array configurations, with baselines of 20–400 m. 1924–292, a blazar, was utilized as a bandpass calibrator and Titan was used for the flux calibration (Bussmann et al. 2013). The effective beam size is $1''.66$ and the rms is 6 mJy beam^{-1} . The SMA continuum is shown in Figure 1 and is used in the lensing model.

The CO $J = 2 \rightarrow 1$ line ($\nu_{\text{rest}} = 230.538 \text{ GHz}$, $\nu_{\text{obs}} = 86.0 \text{ GHz}$ at $z = 1.68$) was detected by the Combined Array for Research in Millimeter-wave Astronomy (CARMA;

Table 2
Photometry of HATLAS J132427

Instrument	λ	S_ν
CHFT (<i>r</i> band)	0.66 μm	$0.05 \pm 0.01 \mu\text{Jy}$
CHFT (<i>z</i> band)	0.98 μm	$0.09 \pm 0.01 \mu\text{Jy}$
<i>HST</i> (F105W)	1.06 μm	$0.79 \pm 0.4 \mu\text{Jy}$
<i>HST</i> (F160W)	1.54 μm	$1.81 \pm 0.6 \mu\text{Jy}$
Keck (<i>H</i> band)	1.63 μm	$2.41 \pm 0.8 \mu\text{Jy}$
Keck (K_s band)	2.20 μm	$3.92 \pm 0.6 \mu\text{Jy}$
WISE W1	3.35 μm	$0.30 \pm 0.01 \text{ mJy}$
WISE W2	4.60 μm	$0.22 \pm 0.01 \text{ mJy}$
WISE W3	11.56 μm	$0.32 \pm 0.03 \text{ mJy}$
WISE W4	22.09 μm	$2.81 \pm 0.7 \text{ mJy}$
<i>Herschel</i> (PACS)	100 μm	$41 \pm 4 \text{ mJy}$
<i>Herschel</i> (PACS)	160 μm	$180 \pm 14 \text{ mJy}$
<i>Herschel</i> (SPIRE)	250 μm	$347 \pm 25 \text{ mJy}$
<i>Herschel</i> (SPIRE)	350 μm	$378 \pm 28 \text{ mJy}$
<i>Herschel</i> (SPIRE)	500 μm	$268 \pm 21 \text{ mJy}$
SCUBA2 JCMT	850 μm	$43 \pm 1.2 \text{ mJy}$
SMA	870 μm	$30.2 \pm 5.2 \text{ mJy}$
PdBI	2 mm	$1.2 \pm 0.1 \text{ mJy}$
CARMA	3.5 mm	$200 \pm 170 \mu\text{Jy}$
VLA	4.3 cm	$350 \pm 30 \mu\text{Jy}$
VLA	21 cm	$1.95 \pm 0.24 \text{ mJy}$

PI: Riechers). The observations were conducted on 2012 November 23 using the D configuration (11–146 m baselines). The beam size was $7'' \times 4.4''$ and a rms noise of $0.76 \text{ mJy beam}^{-1}$. The total on-source time was 2.3 hr while two blazars 1310 + 323 and 0927 + 390 were used to derive the bandpass shape and for complex gain calibration. Figure 4 shows CARMA contours overlaid on the Keck/NIRC2 K_s -band image.

The Canada–Hawaii–France Telescope (CFHT) was used to image HATLAS J132427 in both the *z* (925 nm) and *r* (640 nm) bands (PI: Yee). The integration times for the *r* and *z* bands were 900 s and 600, respectively, and the observations were carried out on 1999 July 5 (Gladders et al. 2003). These observations were used to measure $z = 0.9$ for the foreground cluster.

The Institut de Radioastronomie Millimetrique Plateau de Bure Interferometer (IRAM PdBI) was used to obtain 1.1 hr of on-source time during 2012 November using six 15 m antennas with the D configuration. The frequency was set to 129.028 GHz. The CO $J = 3 \rightarrow 2$ line was detected at 3σ . The flux density measurement is used in the SED analysis.

HATLAS J132427 is detected by the *Wide Field Infrared Survey Explorer* (WISE; Wright et al. 2010) in four bands ranging from $3.35 \rightarrow 22.09 \mu\text{m}$ all used in the SED analysis (Table 2).

4. LENS MODEL

We make use of the program LENSTOOL (Kneib et al. 1996; Jullo et al. 2007) to reconstruct the lensed galaxy and to derive the magnification factors of HATLAS J132427. Using the *HST* F160W high-resolution imaging data, the gravitational potentials contributing to this model are identified using SExtractor (Bertin & Arnouts 1996) with their parameters being optimized by the Bayesian Markov Chain Monte Carlo (MCMC) sampler used in LENSTOOL. For each image (F160W, F105W, K_s , SMA), the whole arc is broken down into four ellipses of varying sizes and brightnesses,

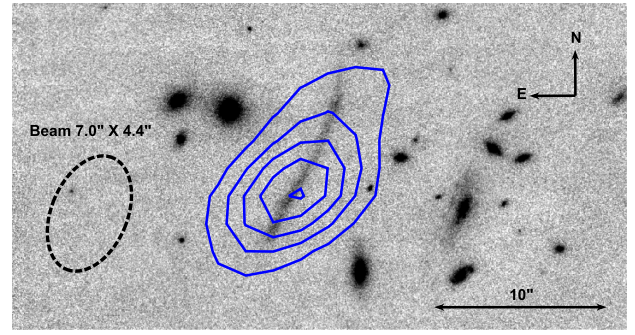


Figure 4. Keck/NIRC2 K_s -band image with CARMA contours overlaid. The contours are at 2σ , 4σ , 6σ , 8σ , and 10σ , where σ is the rms noise ($0.76 \text{ mJy beam}^{-1}$). For reference, we show the CARMA beam size and orientation.

which are created using measured elliptical sizes and flux densities from SExtractor. These ellipses are then passed through the LENSTOOL model to reconstruct the source-plane image.

Figure 2 shows the Keck/NIRC2 K_s -band image, with the gravitational potentials used in the model circled in green and the critical and caustic lines overlaid. From Gladders & Yee (2005), the cluster members used in the model are at photometric $z = 0.997 \pm 0.017$ based on *r*- and *z*-band imaging. We assume a constant mass-to-light ratio and adopt a $0''.5$ uncertainty in the position of the critical lines, which corresponds to the thinnest part of the arc and should account for line-of-sight perturbations. The lens galaxies are modeled using a pseudo-elliptical isothermal mass density profile (PIEMD; Kneib et al. 1996). To create the model, the other sources in the field of unknown redshift were also placed at $z = 0.997$. There are a total of 26 galaxies used in the model, most of which are out of view in the figure and do not contribute significantly to the modeled potential. The cluster members that contribute the largest potential to the model are the galaxies that fall in the blue critical lines in the figure.

Compared with observations, models with multiply imaged systems resulted in lenses that were too large and, thus, unrealistic. Therefore, a model assuming a singly imaged source was utilized. As a main constraint, we assumed that the central thin part of the arc was overlapping the critical line, as has been observed for some very elongated arcs (see the Clone arc in Jones et al. 2010). Placing the critical line closer to the arc results in increased stretching. The arc of HATLAS J132427 is very stretched, thus the critical line must overlap with the arc. However, the critical line cannot cross the arc, otherwise there would be two images.

Figure 5 shows the imaging for four bands F105W, F160W, K_s , and SMA along with their model in the image plane, the residual and the source-plane reconstruction. The long arc is detected in the near-IR bands, with the SMA flux only being detected above 3σ in the southern portion of the arc. The stellar portion of HATLAS J132427 corresponds to the large extended arc, suggesting that it has a higher magnification than the dust portion. The third column of Figure 5 shows the residual after subtracting the model from the image. It is clear that the model that LENSTOOL constructs does not perfectly describe the morphology and does leave residuals. Considering the lack of additional constraints to improve the overall lens model, resulting from a singly imaged source, we accepted that the current model is likely the best we can presently construct.

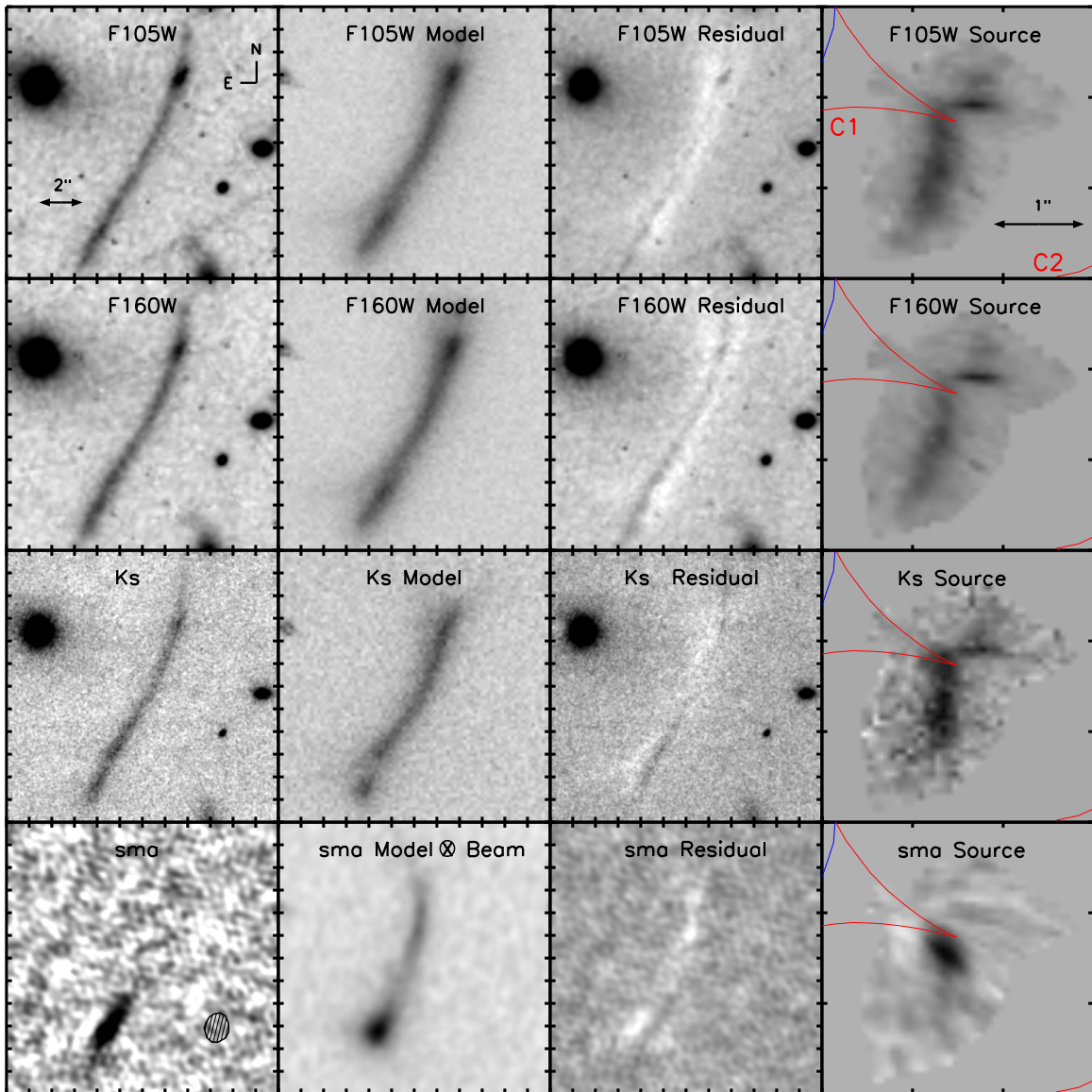


Figure 5. Lens modeling of HATLAS J132427 at several optical/infrared wavelengths and at $870\ \mu\text{m}$. First column: the original imaging for the two *HST* bands, as well as Keck and SMA. The beam size and orientation is overlaid on the SMA frame. Second column: image obtained with the lens model for each band. The SMA model is convolved with a 2D Gaussian model of the SMA beam. Third column: the residual obtained by subtracting the model from the original image. The scale is set to see the areas of over and under subtraction. Fourth column: the source-plane reconstruction for each band, with the critical and caustic lines overlaid in blue and red, respectively. The C1 and C2 refer to the caustic lines as shown in Figure 2.

The best-fit model gives $\mu_{\text{dust}} = 4.9 \pm 1.8$, while the stellar magnification making up the extended arc is $\mu_{\text{stars}} = 15.7 \pm 4.3$. In George et al. (2013), a magnification estimate for the molecular gas is derived following Harris et al. (2012) and Bothwell et al. (2013). Using the $J = 1 \rightarrow 0$ luminosity and the FWHM, μ_{Gas} is found to be ~ 11 . Due to the large uncertainty in the FWHM of the gas (e.g., $640 \pm 270\ \text{km s}^{-1}$) the final estimate of the error for the derived value is ± 7 , which is consistent with the magnification values found with the lens model used here. In Bussmann et al. (2013), a lens model for SMA using two galaxies instead of the two cluster components resulted in a magnification of 2.8 ± 0.4 . The SMA data having just one image in Bussmann et al. 2013 made the model more difficult to constrain, whereas the multi-wavelength model presented here includes SMA, Keck, *HST*, etc. and can be considered a more complete model of the dust magnification.

5. SPECTRAL ENERGY DISTRIBUTION MODELING

The SED of HATLAS J132427 was analyzed using the Multi-wavelength Analysis of Galaxy Physical Properties (MAGPHYS) software (da Cunha et al. 2008). The MAGPHYS package compares the observed flux density values to a library of model SEDs at the same redshift. Here we use the new HIGHZ model library of MAGPHYS SEDs, which was developed to interpret observations of SMGs from the ALESS survey (da Cunha et al. 2015), and should be more appropriate to fit the SEDs of DSFGs at high redshift.

The photometry for CFHT, *HST*, and Keck were done using the SExtractor package (Bertin & Arnouts 1996) using a flexible elliptical aperture to account for the elongated nature of the source. The *WISE* photometry comes from the online *WISE* catalogs. The remaining photometry comes from George et al. (2013) and is discussed in Section 3. Table 2 lists the observed

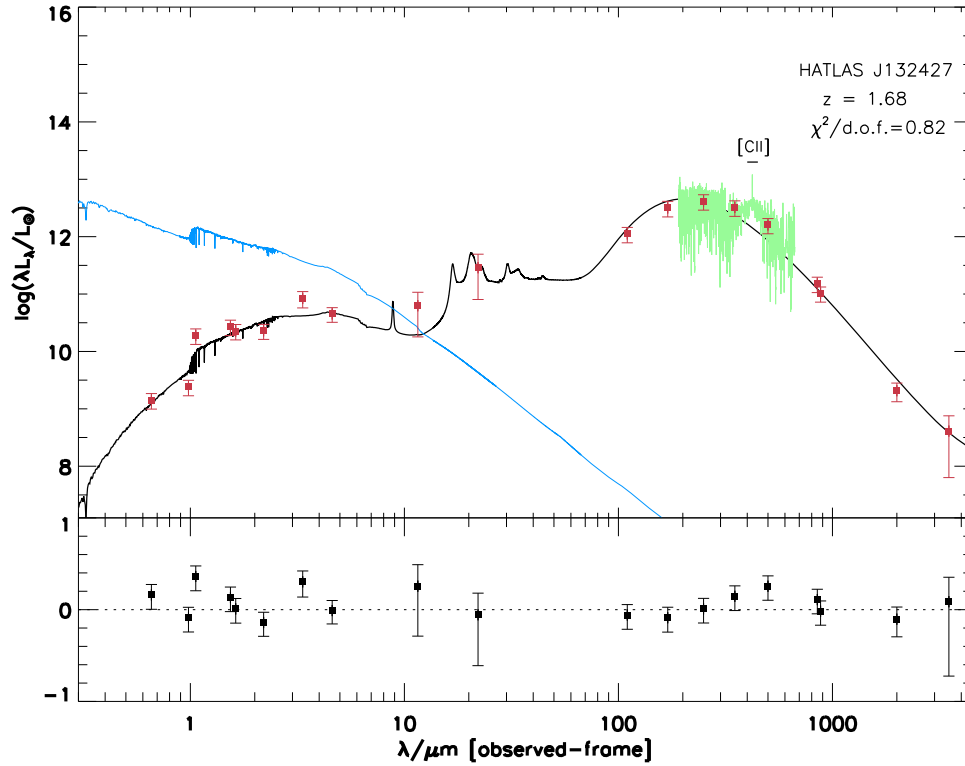


Figure 6. Top: the best-fit SED model is plotted in black while the intrinsic model without dust extinction is plotted in blue. The flux values have been demagnified based on wavelength. The *Herschel* FTS spectrum is shown in green. The FTS spectrum is not used in the SED fit but is shown here for reference. Bottom: the residuals for each fit.

photometry used in the model fit with a spectroscopic redshift of 1.68. Because there is differential magnification for the dust and stellar components (Calanog et al. 2014), the observed fluxes were demagnified based on wavelength. The stellar fluxes corresponding to the full arc in the SED were demagnified by 15.7 ± 4.3 , while the dust portion centered on the lower bright clump was demagnified by 4.9 ± 1.8 .

The *WISE* W3 and W4 bands, at 12 and 22 μm respectively, posed a problem as the MAGPHYS model SED showed those flux densities were a combination of both stellar and dust emission. In order to account for the uncertainty, the error bars were extended to cover the entire magnification range, with flux densities corrected by 10, corresponding to the average of the dust and stellar magnification factors. Several fits were performed using a lower magnification for the W4 band, corresponding to more dust emission, as well as a higher magnification for the W3 band, corresponding to higher stellar contribution; in the end, the average value provided the best fit.

We note that the SMA flux measurements might be underestimated in the fit due to the short baseline coverage of the observations, which could account for the difference between the 870 and 850 μm flux values. This could lead to an underestimate of the SFR, which is correlated with the total dust luminosity (Kennicutt 1998). The dust temperature is also correlated with the dust luminosity (Chapman et al. 2005) and therefore could also be underestimated. The compact configuration of SMA is expected to give an angular resolution of about nine and, considering the large uncertainty and narrow width of the feature, the total flux from SMA should not be resolved out.

Figure 6 shows the final best fit for the SED plotted in black, while the intrinsic model without dust extinction is plotted in

Table 3
SED Fit and Derived Properties

SED fit	
f_{μ} (SFH/IR)	$0.857^{+0.20}_{-0.35}$
A_V	$4.19^{+0.20}_{-0.24}$
M_*	$11.2^{+3.2}_{-3.8} 10^{10} M_{\odot}$
SFR	$390^{+60}_{-57} M_{\odot} \text{ yr}^{-1}$
L_{dust}	$46.8^{+5.6}_{-7.0} 10^{11} L_{\odot}$
M_{dust}	$13.9^{+3.0}_{-2.8} 10^8 M_{\odot}$
T_{dust}	$33.9^{+2.1}_{-1.9} \text{ K}$
sSFR	$30 \pm 2 10^{-10} \text{ yr}^{-1}$
Derived Properties	
μ_{dust}	4.9 ± 1.8
μ_{stars}	16 ± 4.3
$r_{\text{eff Gas}}$	$8.8 \pm 3.7 \text{ kpc}$
$r_{\text{eff Dust}}$	$3.2 \pm 1.2 \text{ kpc}$
Σ_{SFR}	$12.2^{+6.8}_{-6.7} M_{\odot} \text{ yr}^{-1} \text{ kpc}^{-2}$
Σ_{gas}	$347 \pm 200 M_{\odot} \text{ pc}^{-2}$
M_{gas}	$8.6 \pm 3.3 \times 10^{10} \times \alpha_{\text{CO}} M_{\odot}$
Gas Fraction ($M_{\text{gas}}/(M_{\text{star}} + M_{\text{gas}})$)	0.43 ± 0.13

Note.

¹ Based on Narayanan et al. (2012).

blue. The physical properties derived from the SED fit are listed in Table 3. The FTS spectrum, with the [C II] line labeled, is shown for reference and not used in the fit. The χ^2 per degree of freedom is 0.82. The importance of the results of the SED fitting and their derived properties are discussed in the next section.

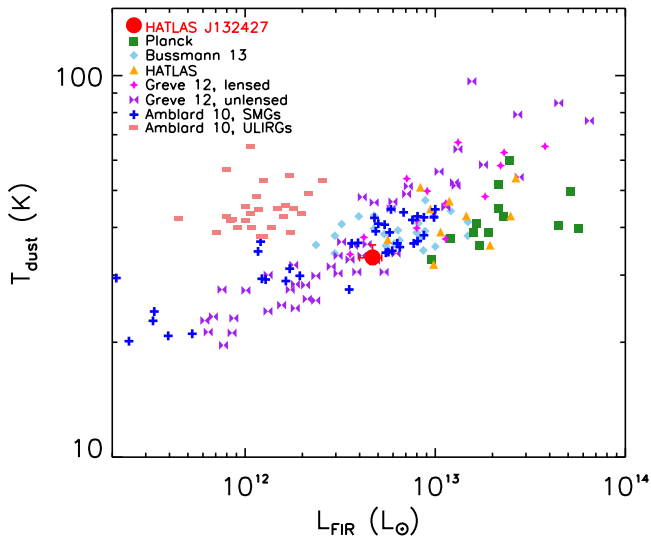


Figure 7. Dust temperature vs. FIR luminosity. For comparison, other lensed and non-lensed galaxies are plotted, including the other *Planck*/*Herschel*-detected lensed galaxies (Canameras et al. 2015), *Herschel* lensed galaxies (Bussmann et al. 2013), as well as other lensed/unlensed SMGs and ULIRGs (Amblard et al. 2010; Greve et al. 2012). To make the comparison more instructive the lensed galaxies have had L_{FIR} demagnified by a factor of five.

6. DISCUSSION

Our knowledge of the physical properties of DSFGs remains limited and the goal of recent studies is to increase our understanding of the starburst phenomena in DSFGs. For this purpose, we examine the various components of the galaxy, including the dust temperature, the ratio of gas to baryons, the SFR, and its density as well as the far-infrared radio correlation. We start with a discussion of the physical properties derived from the SED fit and compare them to other SMGs and DSFGs.

From the SED analysis, the estimated dust temperature is approximately 34 K, which is consistent with *Herschel*-selected galaxies at a similar luminosity (Symeonidis et al. 2013), as well as ALESS SMGs at a similar redshift (da Cunha et al. 2015). In Figure 7, we examine the relationship between dust temperature and FIR luminosity for SMGs as well as local ULIRGs. From Greve et al. (2012), the high FIR luminosity to dust temperature ratio is suggestive of a high magnification factor. In DSFGs, an increased FIR luminosity correlates with an increased dust temperature. Both values come from the SED fit and are in agreement with the other high- z strongly lensed galaxies. Greve et al. (2012) estimate the magnification factor for the lensed galaxies to be a factor of 1–10, which is consistent with the magnification factor ($\mu_{\text{dust}} \sim 5$) from the lens model for HATLAS J132427.

Stellar masses, as derived from SED fits, depend on a few fundamental assumptions such as the assumed star formation histories (SFH), initial mass functions (IMF), and population synthesis models (see Chabrier 2003; Thomas et al. 2005; Davé et al. 2012; Michałowski et al. 2012, 2014; Conroy et al. 2013). These introduce uncertainties in the measured stellar mass which, along with uncertainties introduced by variations in the metallicity, is usually observed as the scatter around the main sequence in the mass-SFR relation (see also Shivaeei et al. 2015; Speagle et al. 2014). Rest-frame H -band absolute magnitude (M_H) can act as a trace of stellar mass that does not depend upon an assumed SFH. In Figure 8, HATLAS J132427 is

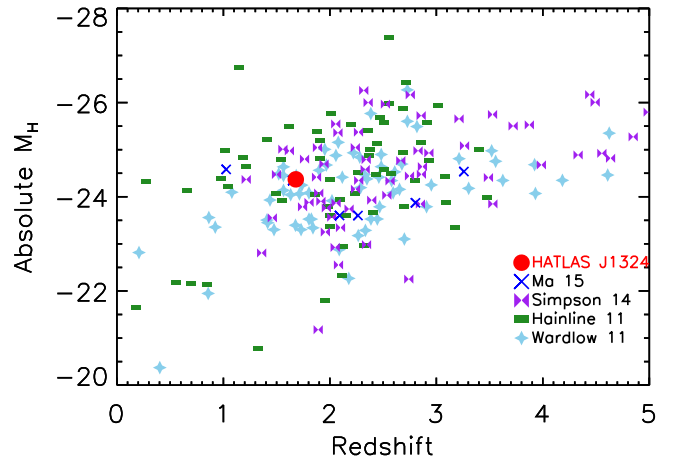


Figure 8. Rest-frame absolute H -band magnitude vs. redshift for DSFGs. The magnitudes have been corrected for magnification. For comparison, DSFGs from other samples are included from Ma et al. (2015), Simpson et al. (2014), Hainline et al. (2011), and Wardlow et al. (2013).

shown to have an M_H consistent with other DSFG samples and likely has a stellar mass consistent with DSFG samples.

To calculate the gas mass, we use the $\text{CO}_{(2-1)}$ luminosity from George et al. (2013) ($\text{CO}_{(2-1)} = 11.3 \pm 1.4 \text{ Jy km s}^{-1}$) and adopt a CO-H_2 conversion factor $\alpha_{\text{CO}} = 1 M_{\odot} (\text{K km s}^{-1} \text{ pc}^2)^{-1}$ consistent with other SMGs (e.g., Tacconi et al. 2008; Hodge et al. 2012). This results in a gas mass of $8.6 \pm 3.3 \times 10^{10} \times (\alpha_{\text{CO}}/1.0) M_{\odot}$, assuming the magnification factor of the gas distribution to be $\mu = 4.9$, consistent with the dust. An alternative calculation for the gas mass comes from Scoville et al. (2014), in which 28 ($z < 3$) SMGs are used to find the ratio of the gas mass to the $850 \mu\text{m}$ luminosity. This ratio is found to be 1.01 ± 0.52 . In Scoville et al. (2014), an α_{CO} of 4.6 is used and so here we scale the ratio down to $\alpha_{\text{CO}} = 1$, giving a final ratio of $L_{850}/M_{\text{ISM}} = 0.22 \pm 0.11$. This ratio gives a gas mass of $7.3 \pm 4.6 \times 10^{10} \times (\alpha_{\text{CO}}/1.0) M_{\odot}$ for HATLAS J132427, which is consistent with the previous result.

The top portion of Figure 9 shows the gas-to-baryon fraction versus stellar mass. For comparison, $z = 1 - 3$ SMGs are plotted as well as $z = 1 - 3$ main-sequence star-forming galaxies. For its stellar mass, HATLAS J132427 has a large gas-to-baryon ratio ($M_{\text{gas}}/(M_{\text{star}} + M_{\text{gas}})$) of 0.43. This is in agreement with other measurements of high- z star-forming galaxies (Tacconi et al. 2013). The green shaded region in Figure 9 shows star-forming galaxies at $z = 2$ from cosmological hydrodynamic simulations (Davé et al. 2010). In Narayanan et al. (2012), it is suggested that α_{CO} is overestimated for systems at high redshift, which could account for some of the scatter. The blue circles on Figure 9 represent the future evolution of HATLAS J132427 assuming a constant SFR and mass conservation. Each blue dot represents a time step of 40 Myr and shows the slope of the evolution as being steeper than the overall trend of the gas fraction versus M_* due to the fact that some gas must be recycled. The bottom portion of Figure 9 shows the SFR versus stellar mass. Also plotted are $z \sim 1$ SMGs and $z \sim 2$ SMGs from the literature for comparison. HATLAS J132427 is above the main-sequence lines for both $z = 1$ (Elbaz et al. 2007) and $z = 2$ (Daddi et al. 2007). This is consistent with the large gas mass of HATLAS J132427 and its being observed in a star-bursting phase. Given the scatter in this relation, the HATLAS J132427 measured mass and star formation is different from the

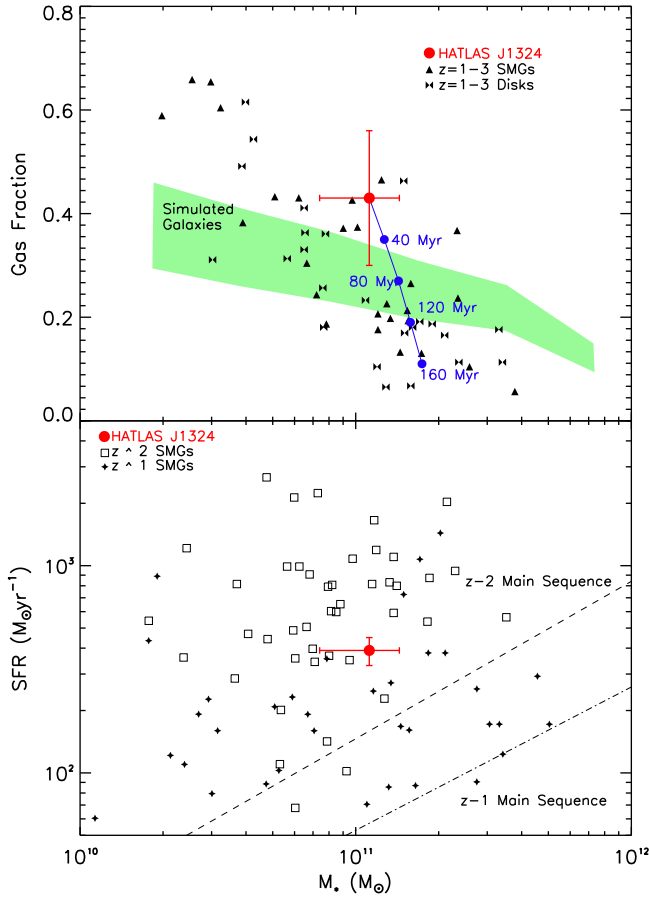


Figure 9. Top: gas fraction vs. stellar mass. The other objects are from Narayanan et al. (2012). The green shaded region represents star-forming galaxies at $z=2$ from cosmological hydrodynamic simulations (Davé et al. 2010). The blue circles represent the evolution of HATLAS J13247 over the course of 160 Myr. Each successive circle represents a 40 Myr time step with a constant SFR and mass conservation. Bottom: star-formation rate vs. stellar mass. For comparison, $z \sim 2$ SMGs are plotted (Fu et al. 2013) as well as $z \sim 1$ SMGs (Michałowski et al. 2010; Tacconi et al. 2010; Banerji et al. 2011; Timmons et al. 2015). The $z=1$ and $z=2$ main sequences (Ma et al. 2015) are also plotted.

underlying star-forming galaxy population and is consistent with SMGs at similar redshifts.

Figure 10 shows the star-formation surface density versus molecular surface density. Plotted for comparison are $z=1-3$ SMGs and SFGs, as well as local ULIRGs and SFGs. The gas area and effective gas radius is calculated using the observed gas area from CARMA and computing a demagnified gas area based on the lens model. The dust area and effective dust radius are calculated by measuring the area of the SMA source-plane reconstruction. The gas consumption time τ_{disk} , which refers to the star-forming disk region can be calculated using the ratio $\tau_{\text{disk}} = \Sigma_{\text{gas}}/\Sigma_{\text{SFR}}$. For HATLAS J13247 the gas consumption time is ~ 10 Myr. The dot-dashed line on the plot represents $\tau_{\text{disk}} = 70$ Myr, which is populated with SMGs and ULIRGs, while the more quiescent star-forming galaxies have $\tau_{\text{disk}} \sim 1.5$ Gyr. This short timescale of star formation for HATLAS J13247 is consistent with other DSFGs.

We investigate the possibility of an AGN contribution to this source by examining the correlation between FIR and 1.4 GHz radio luminosity, which is shown in Figure 11. It is common to define this correlation in terms of a value q , which is defined as $q = \log(L_{\text{IR}}/(3.75 \times 10^{12} \text{ W})) - \log(L_{1.4}/(\text{W Hz}^{-1}))$. A

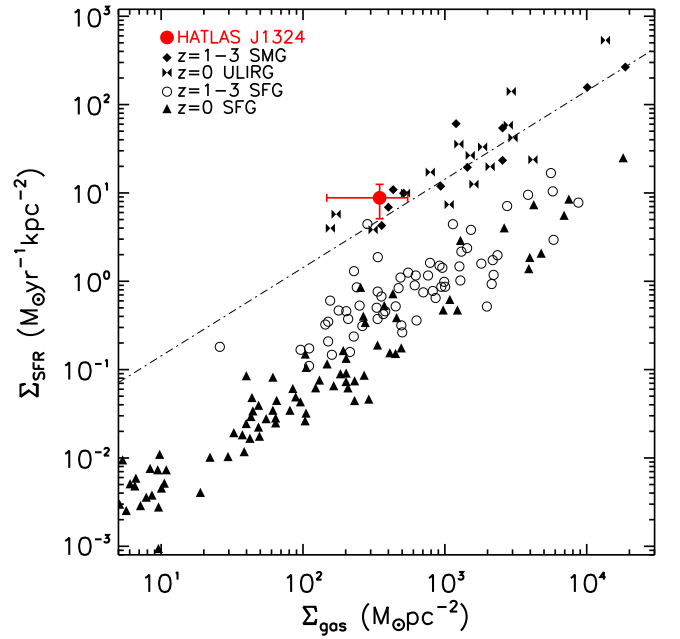


Figure 10. Star formation rate surface density vs. molecular gas surface density for local ULIRGs and SFGs as well as $z \sim 1-3$ SMGs and SFGs. For comparison, SFGs are plotted (Kennicutt 1998), as well as SMGs and local ULIRGs (Fu et al. 2013; Tacconi et al. 2013). The dashed line represents a constant gas consumption ($\tau_{\text{disk}} = \Sigma_{\text{gas}}/\Sigma_{\text{SFR}}$) of 70 Myr for star-forming disks.

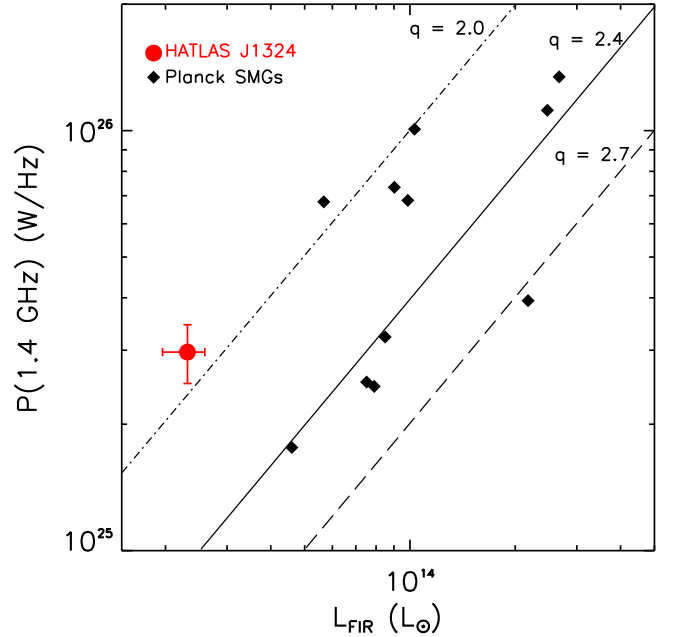


Figure 11. Far-infrared radio correlation for *Planck* and *Herschel* detected lensed DSFGs. The other *Planck*-detected galaxies are from Canameras et al. (2015) and represent the total number of high-redshift lensed galaxies detected in both *Planck* and *Herschel*. The lines represent varying q values ($\log L_{\text{IR}}/(3.75 \times 10^{12} \text{ W}) - \log L_{1.4}/(\text{W Hz}^{-1})$) of 2.0, 2.4, and 2.7.

spectral index $\alpha = -0.8$ is assumed (Condon 1992). The q value for HATLAS J13247 is 1.90, which is lower than the average for DSFGs ~ 2.4 (Ivison et al. 2010). The low q value corresponds to a high relative luminosity in the radio emission and might suggest that HATLAS J13247 has a luminous AGN (e.g., Vlahakis et al. 2007; Bourne et al. 2011). It is

assumed in this calculation that the radio and FIR luminosity are being magnified by the same factor. The output values of MAGPHYS are not strongly affected by AGN contamination (da Cunha et al. 2015). Hayward & Smith (2015) show that strong AGN contamination can lead to an overestimation of the stellar mass in an SED analysis. If the longer wavelength radio is less magnified due to differential lensing, the q value would be underestimated as a result.

7. SUMMARY

HATLAS J132427.0+284452 is a *Herschel* Astrophysical Terahertz Large Area Survey (H-ATLAS) selected strongly lensed arc of length $\sim 15''$ at $z = 1.68$. HATLAS J132427 is also *Planck* detected at 1.30 ± 0.15 Jy in the 350 μm band and is one of a few high- z Planck detections in H-ATLAS. A lens model with source-plane reconstructions at several wavelengths allows the estimation of magnification factors for the stars $\mu_{\text{stars}} \sim 16$ and the dust $\mu_{\text{dust}} \sim 5$. The different magnification values for the dust and stellar components become important for the SED analysis in which the observed fluxes must be demagnified according to wavelength. This source demonstrates the fact that lens models constructed in a single wavelength should not be considered complete due to the effect of differential lensing.

Physical properties of the galaxy are estimated by fitting model SEDs gives a SFR of $\sim 400 M_{\odot} \text{ yr}^{-1}$ and a stellar mass of $\sim 11 \times 10^{10} M_{\odot}$ which are consistent with a high- z dusty star-forming galaxy. The SFR surface density $12 M_{\odot} \text{ yr}^{-1} \text{ kpc}^{-2}$ is high compared to the molecular gas surface density $350 M_{\odot} \text{ pc}^{-2}$. This comes from the lens model reconstruction of the dust area which reveals a large amount of star formation is happening in a single clump. We find that the gas fraction is slightly higher than star-forming galaxies from cosmological hydrodynamic simulations but still consistent with other observations of SMGs at this redshift. The far-infrared radio correlation suggests that HATLAS J132427 might host a luminous AGN, or it might be an artifact of differential lensing.

We wish to thank the anonymous referee whose comments helped improve the paper. Financial support for this work was provided by NASA through grant *HST*-GO-13399 from the Space Telescope Science Institute, which is operated by Associated Universities for Research in Astronomy, Inc., under NASA contract NAS 5-26555. Additional support for N.T., A. C., and H.N. was from NSF through AST-1313319. Some of the data presented herein were obtained at the W.M. Keck Observatory, which is operated as a scientific partnership among the California Institute of Technology, the University of California, and the National Aeronautics and Space Administration. The Observatory was made possible by the generous financial support of the W.M. Keck Foundation. The authors wish to recognize and acknowledge the very significant cultural role and reverence that the summit of Mauna Kea has always had within the indigenous Hawaiian community. We are most fortunate to have the opportunity to conduct observations from this mountain. The Submillimeter Array is a joint project between the Smithsonian Astrophysical Observatory and the Academia Sinica Institute of Astronomy and Astrophysics and is funded by the Smithsonian Institution and the Academia Sinica. C.F. acknowledges funding from CAPES (proc. 12203–1). J.G.N. acknowledges financial support from the Spanish MINECO for a Ramon y Cajal fellowship. H.M.

acknowledges support from the Fundação para a Ciência e a Tecnologia (FCT) through the Fellowship SFRH/BPD/97986/2013. I.O. acknowledges support from the European Research Council in the form of the Advanced Investigator Programme, 321302, COSMICISM. D.A.R. acknowledges support from the National Science Foundation under grant number AST-1614213 to Cornell University.

REFERENCES

- Amblard, A., Cooray, A., Serra, P., et al. 2010, *A&A*, **518**, L9
 Banerji, M., Chapman, S. C., Smail, I., et al. 2011, *MNRAS*, **418**, 1071
 Bertin, E., & Arnouts, S. 1996, *A&AS*, **117**, 393
 Bothwell, M. S., Smail, I., Chapman, S. C., et al. 2013, *MNRAS*, **429**, 3047
 Bourne, N., Dunne, L., Ivison, R. J., et al. 2011, *MNRAS*, **410**, 1155
 Bussmann, R. S., Pérez-Fournon, I., Amber, S., et al. 2013, *ApJ*, **779**, 25
 Calanog, J. A., Fu, H., Cooray, A., et al. 2014, *ApJ*, **797**, 138
 Canameras, R., Nesvadba, N. P. H., Guery, D., et al. 2015, arXiv:1506.01962
 Casey, C. M., Narayanan, D., & Cooray, A. 2014, *PhR*, **541**, 45
 Chabrier, G. 2003, *PASP*, **115**, 763
 Chapman, S. C., Blain, A. W., Smail, I., & Ivison, R. J. 2005, *ApJ*, **622**, 772
 Condon, J. J. 1992, *ARA&A*, **30**, 575
 Conroy, C., Dutton, A. A., Graves, G. J., Mendel, J. T., & van Dokkum, P. G. 2013, *ApJL*, **776**, L26
 da Cunha, E., Charlot, S., & Elbaz, D. 2008, *MNRAS*, **388**, 1595
 da Cunha, E., Walter, F., Smail, I. R., et al. 2015, *ApJ*, **806**, 110
 Daddi, E., Dickinson, M., Morrison, G., et al. 2007, *ApJ*, **670**, 156
 Davé, R., Finlator, K., & Oppenheimer, B. D. 2012, *MNRAS*, **421**, 98
 Davé, R., Finlator, K., Oppenheimer, B. D., et al. 2010, *MNRAS*, **404**, 1355
 Eales, S., Dunne, L., Clements, D., et al. 2010, *PASP*, **122**, 499
 Elbaz, D., Daddi, E., Le Borgne, D., et al. 2007, *A&A*, **468**, 33
 Fu, H., Cooray, A., Feruglio, C., et al. 2013, *Natur*, **498**, 338
 Fu, H., Jullo, E., Cooray, A., et al. 2012, *ApJ*, **753**, 134
 George, R. D., Ivison, R. J., Hopwood, R., et al. 2013, *MNRAS*, **436**, L99
 Gladders, M. D., Hoekstra, H., Yee, H. K. C., Hall, P. B., & Barrientos, L. F. 2003, *ApJ*, **593**, 48
 Gladders, M. D., & Yee, H. K. C. 2005, *ApJS*, **157**, 1
 González-Nuevo, J., Lapi, A., Fleuren, S., et al. 2012, *ApJ*, **749**, 65
 Greve, T. R., Vieira, J. D., Weiß, A., et al. 2012, *ApJ*, **756**, 101
 Griffin, M. J., Abergel, A., Abreu, A., et al. 2010, *A&A*, **518**, L3
 Hainline, L. J., Blain, A. W., Smail, I., et al. 2011, *ApJ*, **740**, 96
 Harris, A. I., Baker, A. J., Frayer, D. T., et al. 2012, *ApJ*, **752**, 152
 Hayward, C. C., & Smith, D. J. B. 2015, *MNRAS*, **446**, 1512
 Hodge, J. A., Carilli, C. L., Walter, F., et al. 2012, *ApJ*, **760**, 11
 Holland, W. S., Bintley, D., Chapin, E. L., et al. 2013, *MNRAS*, **430**, 2513
 Ivison, R. J., Magnelli, B., Ibar, E., et al. 2010, *A&A*, **518**, L31
 Ivison, R. J., Papadopoulos, P. P., Smail, I., et al. 2011, *MNRAS*, **412**, 1913
 Jones, T., Ellis, R., Jullo, E., & Richard, J. 2010, *ApJL*, **725**, L176
 Jullo, E., Kneib, J.-P., Limousin, M., et al. 2007, *NJPh*, **9**, 447
 Kennicutt, R. C., Jr. 1998, *ARA&A*, **36**, 189
 Kneib, J.-P., Ellis, R. S., Smail, I., Couch, W. J., & Sharples, R. M. 1996, *ApJ*, **471**, 643
 Kümmel, M., Walsh, J. R., Pirzkal, N., Kuntschner, H., & Pasquali, A. 2009, *PASP*, **121**, 59
 Lapi, A., González-Nuevo, J., Fan, L., et al. 2011, *ApJ*, **742**, 24
 Lawrence, A., Warren, S. J., Almaini, O., et al. 2007, *MNRAS*, **379**, 1599
 Le Floc'h, E., Papovich, C., Dole, H., et al. 2005, *ApJ*, **632**, 169
 Lilly, S. J., Eales, S. A., Gear, W. K. P., et al. 1999, *ApJ*, **518**, 641
 Ma, B., Cooray, A., Calanog, J. A., et al. 2015, *ApJ*, **814**, 17
 Messias, H., Dye, S., Nagar, N., et al. 2014, *A&A*, **568**, A92
 Michałowski, M., Hjorth, J., & Watson, D. 2010, *A&A*, **514**, A67
 Michałowski, M. J., Dunlop, J. S., Cirasuolo, M., et al. 2012, *A&A*, **541**, A85
 Michałowski, M. J., Hayward, C. C., Dunlop, J. S., et al. 2014, *A&A*, **571**, A75
 Narayanan, D., Bothwell, M., & Davé, R. 2012, *MNRAS*, **426**, 1178
 Nayyeri, H., Keele, M., Cooray, A., et al. 2016, arXiv:1601.03401
 Negrello, M., Hopwood, R., De Zotti, G., et al. 2010, *Sci*, **330**, 800
 Negrello, M., Perrotta, F., González-Nuevo, J., et al. 2007, *MNRAS*, **377**, 1557
 Planck Collaboration, Ade, P. A. R., Aghanim, N., et al. 2011, *A&A*, **536**, A1
 Poglitsch, A., Waelkens, C., Geis, N., et al. 2010, *A&A*, **518**, L2
 Riechers, D. A., Hodge, J., Walter, F., Carilli, C. L., & Bertoldi, F. 2011, *ApJL*, **739**, L31
 Scoville, N., Aussel, H., Sheth, K., et al. 2014, *ApJ*, **783**, 84
 Shivaee, I., Reddy, N. A., Shapley, A. E., et al. 2015, *ApJ*, **815**, 98
 Simpson, J. M., Swinbank, A. M., Smail, I., et al. 2014, *ApJ*, **788**, 125

- Speagle, J. S., Steinhardt, C. L., Capak, P. L., & Silverman, J. D. 2014, *ApJS*, **214**, 15
- Swinbank, A. M., Chapman, S. C., Smail, I., et al. 2006, *MNRAS*, **371**, 465
- Symeonidis, M., Vaccari, M., Berta, S., et al. 2013, *MNRAS*, **431**, 2317
- Tacconi, L. J., Genzel, R., Neri, R., et al. 2010, *Natur*, **463**, 781
- Tacconi, L. J., Genzel, R., Smail, I., et al. 2008, *ApJ*, **680**, 246
- Tacconi, L. J., Neri, R., Genzel, R., et al. 2013, *ApJ*, **768**, 74
- Thomas, D., Maraston, C., Bender, R., & Mendes de Oliveira, C. 2005, *ApJ*, **621**, 673
- Timmons, N., Cooray, A., Nayyeri, H., et al. 2015, *ApJ*, **805**, 140
- Vlahakis, C., Eales, S., & Dunne, L. 2007, *MNRAS*, **379**, 1042
- Wardlow, J. L., Cooray, A., De Bernardis, F., et al. 2013, *ApJ*, **762**, 59
- Wizinowich, P. L., Le Mignant, D., Bouchez, A. H., et al. 2006, *PASP*, **118**, 297
- Wright, E. L., Eisenhardt, P. R. M., Mainzer, A. K., et al. 2010, *AJ*, **140**, 1868
- Younger, J. D., Fazio, G. G., Wilner, D. J., et al. 2008, *ApJ*, **688**, 59